

# Multifunctional volumetric meta-optics for color and polarization image sensors: supplementary material

PHILIP CAMAYD-MUÑOZ, CONNER BALLEW, GREGORY ROBERTS, ANDREI FARAON\*

Kavli Nanoscience Institute and Thomas J. Watson Sr. Laboratory of Applied Physics, California Institute of Technology, Pasadena, California 91125

\*Corresponding author: [faraon@caltech.edu](mailto:faraon@caltech.edu)

Published 31 March 2020

This document provides supplementary information to "Multifunctional volumetric meta-optics for color and polarization image sensors," <https://doi.org/10.1364/OPTICA.384228>.

## I. Inverse design method

In this work we design three-dimensional dielectric structures, optimized to perform a specified optical scattering function: in this case, focusing incident plane waves to different positions depending on the frequency and polarization. The structure is defined by a spatially-dependent refractive index distribution  $n(\vec{x})$  within a cubic design region. This represents an expansive design space with the capacity to express a broad range of complex optical multifunctionality. However, identifying the optimal index distribution for a given target function remains a challenging inverse design problem, particularly for strongly scattering devices [1]. Therefore, we adopt an iterative approach guided by gradient descent (Fig. S1) in order to efficiently generate complex 3D designs [2]: starting from an initial index distribution, we use full-wave simulations (FDTD) to calculate the sensitivity of the sorting efficiency with respect to perturbations of the refractive index. The sensitivity can be calculated from just two simulations, allowing efficient optimization of three-dimensional devices with modest resources. Based on the sensitivity, we modify the initial design in order to maximize the performance while conforming to fabrication constraints. This update process is repeated until the optimized device can efficiently perform the target function.

For the designs presented in this manuscript, we start with a uniform refractive index distribution,  $n_0(\vec{x}) = \frac{1}{2}(n_{\max} + n_{\min})$ . This distribution is continually updated to maximize the electromagnetic intensity at the target location in the focal plane,  $f(n(\vec{x})) = |\vec{E}(\vec{x}_0)|^2$ . This figure of merit serves as a proxy for sorting efficiency while simplifying the sensitivity calculation. The

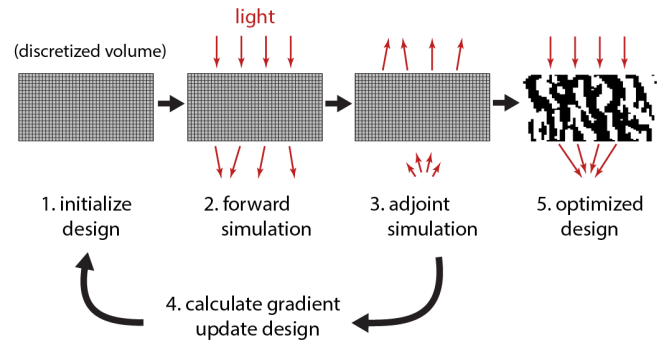


**Fig. S1.** Scattering elements are tailored to perform a target function through gradient descent. Starting from an initial design, we compute the sensitivity of the sorting efficiency to changes in the refractive index using a pair of FDTD simulations. The design is then updated in proportion to the sensitivity. After many iterations, the resulting structure focuses incident light with high efficiency.

sensitivity,  $\frac{df}{dn}(\vec{x})$ , is computed from the electromagnetic fields in two FDTD simulations:

$$\frac{df}{dn}(\vec{x}) = 2n(\vec{x}) \text{Re}\{\vec{E}_{fwd} \cdot \vec{E}_{adj}\} \quad (\text{S1})$$

where  $\vec{E}_{fwd}$  are the electric fields within the cube when illuminated from above with a plane wave, and  $\vec{E}_{adj}$  are the electric fields within the cube when illuminated from below with a point source at the target location. The phase and amplitude of the point source are given by the electric field at the target location in the forward simulation. We simultaneously calculate the sensitivity for multiple

incident wavelengths and polarizations across the visible spectrum, assigning each spectral band to a different quadrant: red (600 nm – 700 nm) green (500 nm – 600 nm) and blue (400 nm – 500 nm). Then we use the spectrally-averaged sensitivity to update the refractive index of the device:

$$n_{i+1}(\vec{x}) = n_i(\vec{x}) + \alpha \sum_{\lambda} \frac{df_{\lambda}}{dn}(\vec{x}) \quad (\text{S2})$$

The step size  $\alpha$  fixed at a small fraction (typically  $\alpha = 0.001$ ) to ensure that the change in refractive index can be treated as a perturbation in the linear regime. The sensitivity is recalculated after each update.

## II. Fabrication constraints

### A. Binary index

During the optimization process, we directly enforce a set of constraints on the index distribution as required by the fabrication process. In particular, we are designing high-contrast scattering elements constructed from two materials. Although the gradient descent algorithm detailed above produces optimized devices with gradient index, we can enforce the binary condition by introducing an auxiliary density  $\rho(\vec{x})$  ranging from [0,1]. The density is related to the refractive index distribution via a sigmoidal projection filter [3]:

$$n(\vec{x}) = P(\rho(\vec{x})) = \left( \frac{1}{2} + \frac{\tanh(2\beta\rho(\vec{x}) - \beta)}{2 \tanh(\beta)} \right) (n_{\max} - n_{\min}) + n_{\min} \quad (\text{S3})$$

where the parameter  $\beta$  controls the filter strength. For small  $\beta$ , the index distribution is equal to the density scaled to the range of available refractive index. For large  $\beta$ , the sigmoid filter approximates a Heaviside function, and the index distribution is pushed toward either extreme. Importantly, the filter function is continuously differentiable, such that the sensitivity can be written in terms of the density:  $\frac{df}{d\rho} = \frac{df}{dn} \frac{dn}{d\rho}$ . During optimization we can parameterize the design using the density  $\rho(\vec{x})$  and  $\beta$ , gradually increasing the strength of the filter. At early stages and small  $\beta$ , this is equivalent to the unfiltered case. Over time as the strength increases, the optimized index distribution is gradually pushed toward a binary design, even as the density remains continuous.

### B. Minimum feature size

In addition to material constraints, device designs must conform to the resolution limits imposed by the fabrication process. For example, diffraction and proximity dosing effects limit electron beam lithography to approximately 10 nm features. We enforce this minimum feature size for device designs by introducing a “dilated” density  $\tilde{\rho}(\vec{x})$ , which represents the maximum density  $\rho(\vec{x}')$  within a neighborhood  $\Omega$  of each point  $\vec{x}$  [4].

$$\tilde{\rho}(\vec{x}) = D(\rho(\vec{x})) = \sqrt[M]{\frac{1}{M} \sum_{\Omega} (\rho(\vec{x}'))^M} \quad (\text{S4})$$

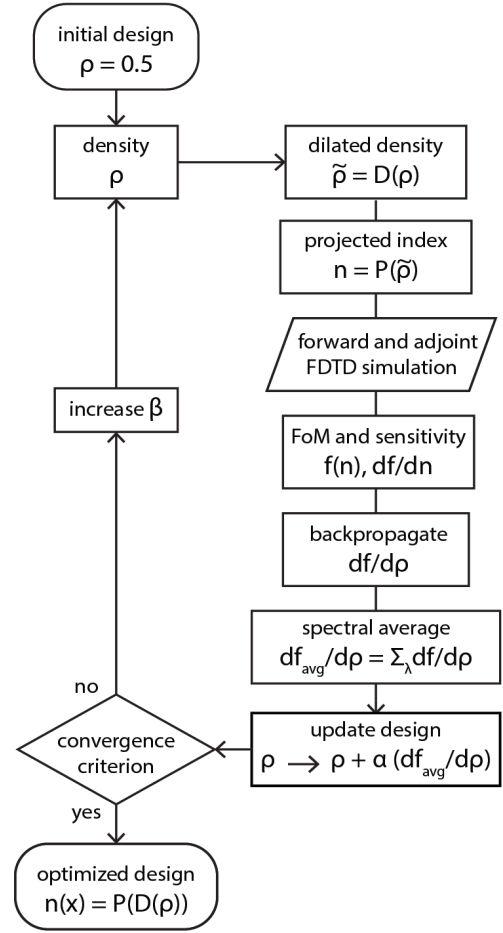


**Fig. S2.** The design of optimized scattering elements consists of iterative updates to the refractive index distribution, guided by the sensitivity to perturbations in the index, and constrained by materials and fabrication processes as outlined above.

For a sufficiently large exponent  $M$ , this operation approximates morphological grayscale dilation. However it is continuously differentiable with respect to the arguments. Therefore, the sensitivity can be written in terms of the un-dilated density:  $\frac{df}{d\rho(\vec{x})} = \frac{df}{d\rho(\vec{x})} = \sum_{\Omega} \frac{df}{d\rho(\vec{x}')} \frac{d\rho(\vec{x}')}{d\rho(\vec{x})}$ . The neighborhood  $\Omega$  is taken to be a circle, where the radius represents the minimum feature size.

When combined with the projection filter, the dilation operation eliminates small features in the final binary index distribution. During optimization, the device is parameterized by the density  $\rho(\vec{x})$ , while the index is defined by the dilated density

$$\tilde{\rho}(\vec{x}):$$

$$n(\vec{x}) = P(\tilde{\rho}(\vec{x})) = P(D(\rho(\vec{x}))) \quad (\text{S5})$$

The neighborhood  $\Omega$  is taken to be a circle, where the radius represents the minimum feature size.

### C. Connected layered designs

Some of the device designs are intended for fabrication by multi-layer 2D lithography, consisting of several patterned slabs that are invariant in the vertical direction (Fig. 2,3). In this case, we restrict the optimization by averaging the calculated sensitivity in the vertical direction within each layer. In effect, voxels within each layer are governed by a shared 2D profile.

For the microwave device (Fig. 3), the design is further constrained so that each layer is fully connected with no floating pieces. We directly impose connectivity by periodically adding bridges between disconnected islands within each layer. This intervention does not take sensitivity into account, and typically causes a small decrease in device performance. Therefore, we only apply the connectivity constraint once per 40 iterations, allowing the performance to recover thereafter.

### III. Sorting efficiency of 3D printed design

The freeform scattering element shown in Fig. 1 is designed for high-resolution 3D printing. It consists of a monolithic polymer cube (index = 1.56), infiltrated by a series of holes (Fig. S3a). As with all the designs presented in this manuscript, the device sorts incident light to different locations depending on the wavelength and polarization. Here we show the sorting efficiency under linearly polarized illumination. The visible spectrum is divided into three spectral bands (400 nm – 500 nm, 500 nm – 600 nm, 600 nm – 700 nm), each focused on a different quadrant in the focal plane (Fig. S3b). We impose mirror symmetry along a diagonal plane bisecting the red and blue quadrants. This guarantees that the green spectral band will focus orthogonal polarizations to opposite quadrants, while the red and blue spectral bands will be polarization independent. Fig. S3c shows the sorting efficiency for each quadrant across the visible spectrum, defined as the fraction of incident optical power that reaches the target quadrant. This design achieves greater efficiency than similar layered devices (Fig. 2d), which impose stronger restrictions on the device topology.

### IV. Dependence on device thickness

Efficient multifunctional devices require a large number of optical degrees of freedom, which scales with the overall device thickness. In the case of spectral- and polarization sorting elements, this restricts the performance of ultrathin devices. Here we show how complex sorting behavior emerges with increased device thickness. Fig. S4 shows the sorting efficiency of several layered devices (similar to Fig. 2), optimized with overall thicknesses ranging from 400 nm – 2000 nm. Thin devices are unable to effectively sort incident light. As thickness increases, the efficiency improves while crosstalk is minimized. We believe that adding even more layers than shown here will increase the performance of the optimized device although not indefinitely. The effect of the number of layers used as well as the thickness of the individual layers is an interesting topic for future investigation.

### V. Dependence on incident angle

The devices presented in this manuscript were designed to sort light at normal incidence. In realistic imaging systems, the illumination will span a range of angles that depends on the numerical aperture of the imaging optics. For example, a typical smartphone camera [5] has a numerical aperture of  $NA = 0.21$ , corresponding to an acceptance cone spanning  $\pm 7.8^\circ$  in  $\text{SiO}_2$ . In

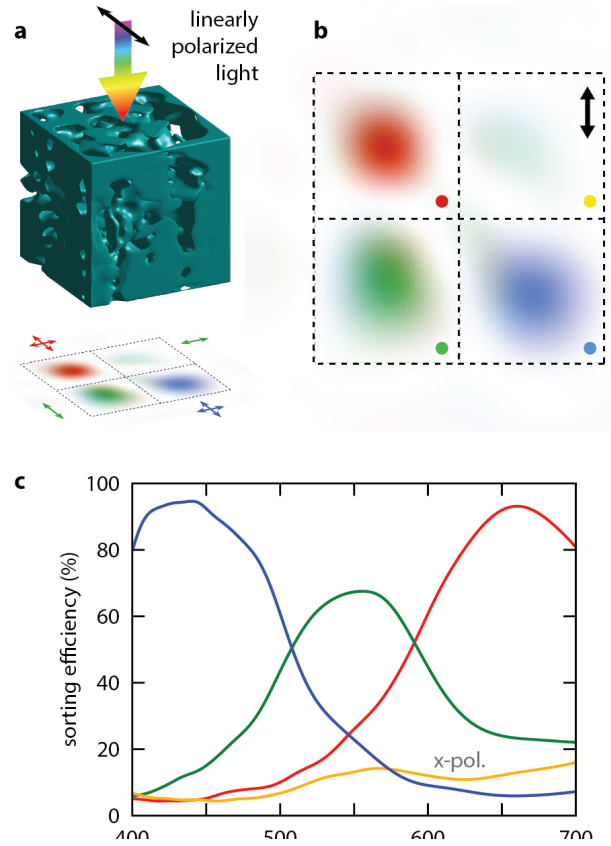


**Fig. S3.** Sorting efficiency of 3D printed scattering element. (a) Device consists of a single piece of polymer, as shown in Fig. 1. Light incident from above is focused to different quadrants depending on the polarization and frequency. (b) Intensity distribution at the focal plane under broadband, linearly polarized illumination. Colors correspond to the observed hue for visible light. The upper right quadrant is assigned to cross-polarized illumination, and therefore remains dark. (c) Sorting efficiency for each of the four focal regions, defined as the fraction of incident light focused into the target quadrant.

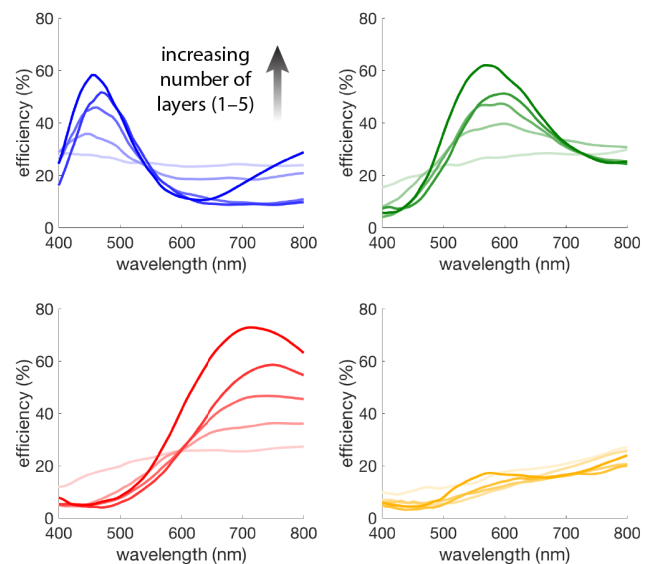


**Fig. S4.** Sorting efficiency for increasing device thickness. Efficiency spectra for the multilayer designs shown in Fig. 2, optimized for 1–5 device layers. Each plot corresponds to a different focal region, including the cross-polarized sub-pixel shown in yellow. Darker lines indicate increasing device thickness.

order to evaluate the device performance under realistic conditions, we have characterized the sorting efficiency of the layered design (shown in Fig. 2) for different illumination angles. As the angle deviates from the surface normal the efficiency decreases (Fig. S5). This is due to an increase in scattering into non-targeted quadrants within the focal plane, as well as reflection from the surface. The drop-off in performance with incident angle is a consequence of decorrelation in the angular scattering through disordered media [6], which scales with the thickness of the scattering medium. Since the device maintains high performance near normal incidence, we define the steepest functional angle where the performance drops to half of the maximum efficiency, roughly  $\pm 8^\circ$ . Therefore, this design may be deployed in color and polarization filters in mobile imaging systems. The range of incidence angles can be extended to steeper angles by reducing the device thickness. Furthermore, we may directly include non-normal incidence into the design algorithm [2], which has so far only considered normal incidence.

## VI. Microwave near field measurement

We sample the scattered microwave near field in the  $K_a$  band using a scanning antenna. An incident Gaussian beam (FWHM = 25 mm) is generated by a vector network analyzer coupled to free space via a microwave horn antenna and focusing mirror (Fig. S6). The input beam passes through the cube, scattering into the far field. We sample the local electric field at a measurement plane 62 mm beyond the output aperture of the device using a WR-28 waveguide flange in order to recover the complex scattering amplitude  $S_{21}$ . By scanning the position of the probe antenna in the measurement plane, we can measure the local electric field profile. We apply a deconvolution filter to account for the anisotropy of the probe and the finite aperture of the device. The complex fields are computationally back-propagated to the focal plane of the device. This analysis is repeated for a range of microwave frequencies within the  $K_a$  band (26–40 GHz), and for both orthogonal polarizations of the input beam. To measure the scattering parameters for an orthogonal polarization, we rotate the device  $90^\circ$ . We also measure the cross-polarized fields by rotating the waveguide flange  $90^\circ$ .

## VII. Power flow analysis

We experimentally validate the design of volumetric scattering elements using a microwave analog by measuring the scattered fields. This analysis reveals close agreement between simulated and measured sorting efficiencies, roughly 40% across the measurement spectrum. However, the performance is lower than previously designed devices (Fig. 1 and 2). Here we account for the remaining energy that is lost in the system. From full-wave simulations we can quantify four sources of loss: reflection from the device, oblique scattering away from the focal plane, and absorption within the material (Fig. S7a). Both reflection and oblique scattering contribute equally to the overall loss in the system, independent of wavelength (Fig. S7b). We believe that these losses can be significantly mitigated by explicitly including them in the optimization algorithm, or through the appropriate choice of boundary conditions and anti-reflection coatings. Due to the agreement between simulated and experimental efficiencies, we conclude that absorption plays a negligible role, which is consistent with the extremely low extinction coefficient of polypropylene in the  $K_a$  band [7].

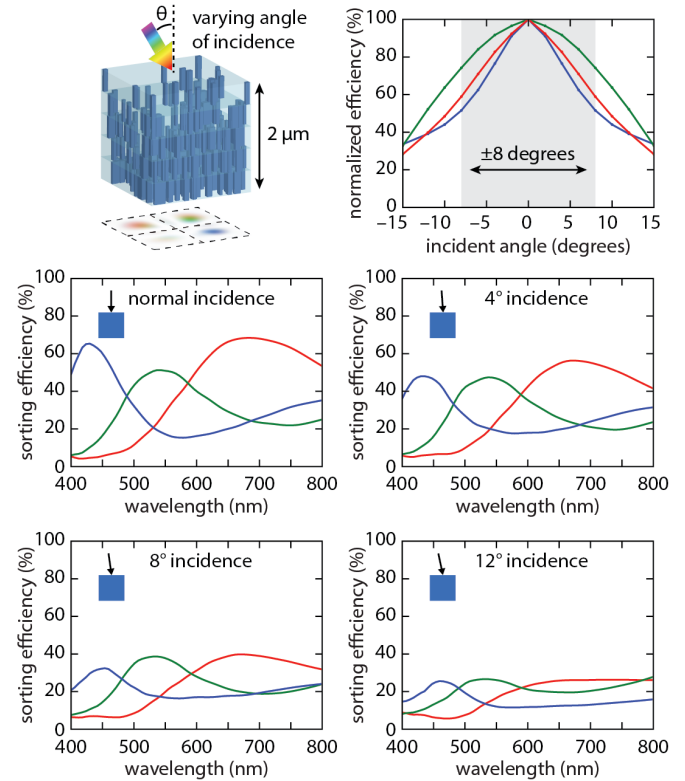


**Fig. S5.** Sorting performance at non-normal incidence. The layered device is optimized to sort light incident from above. The sorting performance degrades as the incident angle increases. Compared to the design at normal incidence, the efficiency is reduced by half at angles beyond  $\pm 8^\circ$ .

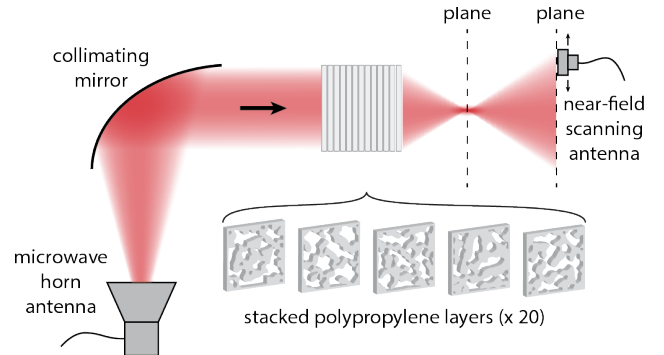


**Fig. S6.** Experimental characterization at microwave frequencies. Microwave device consists of 20 patterned polypropylene sheets, assembled into a cube. The cube is illuminated by a collimated microwave source operating in the  $K_a$  band (26.5 – 40 GHz). Local electric fields are collected by a scanning near-field probe, and back-propagated to the focal plane.

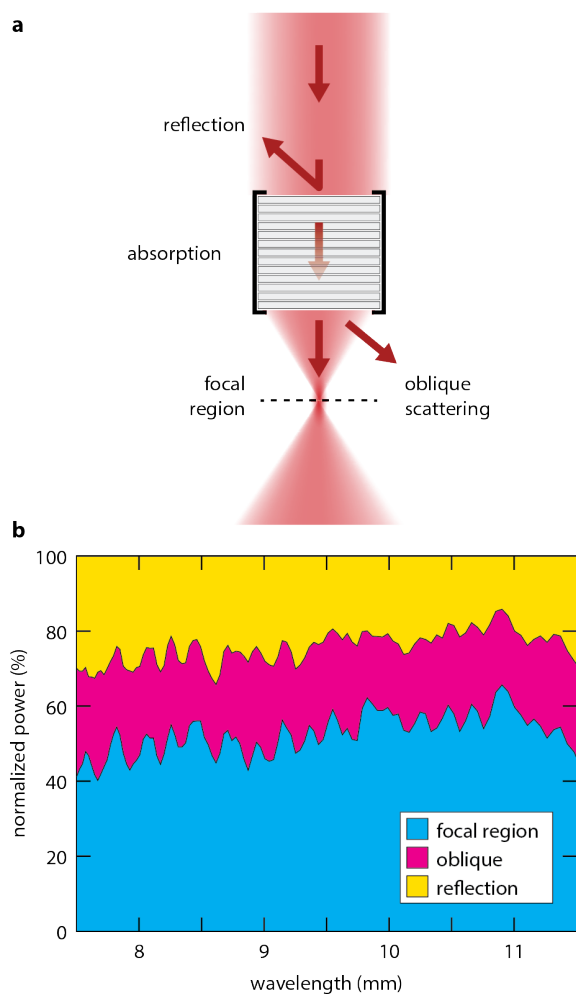


**Fig. S7.** Power flow analysis of microwave devices. (a) The incident microwave beam is deflected into different regions, contributing to lower overall sorting efficiency. (b) Distribution of optical power in simulations, including transmission, reflection, and oblique scattering. The power is normalized to the input aperture of the device.

## References

1. T. D. Gerke and R. Piestun, "Aperiodic volume optics," *Nat. Photonics* **4**, 188–193 (2010).
2. D. Sell, J. Yang, S. Doshay, R. Yang, and J. A. Fan, "Large-Angle, Multifunctional Metagratings Based on Freeform Multimode Geometries," *Nano Lett.* **17**, 3752–3757 (2017).
3. F. Wang, B. S. Lazarov, and O. Sigmund, "On projection methods, convergence and robust formulations in topology optimization," *Struct. Multidiscip. Optim.* **43**, 767–784 (2011).
4. J. K. Guest, J. H. Prévost, and T. Belytschko, "Achieving minimum length scale in topology optimization using nodal design variables and projection functions," *Int. J. Numer. Methods Eng.* **61**, 238–254 (2004).
5. N. A. Switz, M. V. D'Ambrosio, and D. A. Fletcher, "Low-Cost Mobile Phone Microscopy with a Reversed Mobile Phone Camera Lens," *PLoS One* **9**, e95330 (2014).
6. I. Freund, M. Rosenbluh, and S. Feng, "Memory effects in propagation of optical waves through disordered media," *Phys. Rev. Lett.* **61**, 2328–2331 (1988).
7. J. Krupka, "Measurements of the Complex Permittivity of Low Loss Polymers at Frequency Range from 5 GHz to 50 GHz," *IEEE Microw. Wirel. Components Lett.* **26**, 464–466 (2016).